



CHALMERS
UNIVERSITY OF TECHNOLOGY

Local Structure and Entropic Stabilization of Ca-Based Molten Salt Electrolytes

Downloaded from: <https://research.chalmers.se>, 2025-02-07 22:13 UTC

Citation for the original published paper (version of record):

Timhagen, J., Cruz Cardona, C., Weidow, J. et al (2024). Local Structure and Entropic Stabilization of Ca-Based Molten Salt Electrolytes. *Batteries and Supercaps*, 7(12).
<http://dx.doi.org/10.1002/batt.202400297>

N.B. When citing this work, cite the original published paper.

Local Structure and Entropic Stabilization of Ca-Based Molten Salt Electrolytes

Johanna Timhagen,^[a] Carolina Cruz,^[a] Jonathan Weidow,^[a] and Patrik Johansson^{*[a, b]}

Here molten salt electrolytes (MSEs) and specifically their physico-chemical properties as a function of composition are reported on, with a special emphasis on the compositional entropy and targeting calcium battery application. By using MSEs, several problematic issues associated with organic electrolytes, such as the blocking of Ca²⁺ transfer at the electrode/electrolyte interfaces and electrolyte flammability, are avoided. Ca(FSI)₂ salt in combination with the analogous Li-, Na-, and KFSI salts are used in equimolar compositions to first create several ternary MSEs, melting at (ca.) 60–75 °C, a melting temperature which is further reduced to (ca.) 55 °C for the

unique quaternary MSE. This is ascribed to an increased entropy of mixing, which also contributes to an improved stability (re-)crystallization, as shown by Raman spectroscopy. Furthermore, molecular dynamics simulations of the quaternary MSE alongside density functional theory calculations targeting the ion-ion interactions are used to elucidate the local structure in more detail, demonstrating that both the ionic radii and valence influence the coordination and solvation of the cations. These MSEs are stepping-stones towards completely solvent-free, semi-solid, and ideally room-temperature Ca-conducting electrolytes.

Introduction

Calcium is in principle a very attractive metal anode for rechargeable batteries due to the large abundance of calcium in the Earth's crust, its low electrochemical potential,^[1] and its low cost.^[2] Until rather recently,^[3] however, stable plating and stripping of Ca and hence rechargeability of Ca-batteries (CaBs) was deemed impossible, due to the stable phases formed at the electrolyte/electrode interface, completely blocking Ca²⁺ transfer.^[4] Since the pivotal breakthrough, accomplished by using a liquid electrolyte at elevated temperature,^[3] CaBs have attracted significantly more interest,^[5–8] but they are still in their very infancy and new battery designs – such as using novel electrolyte concepts^[9] – are needed to achieve stable cycling of Ca metal anodes, and in the end performant CaBs.

The concepts for Ca conducting electrolytes typically stay in the one salt and one solvent region, even if designs with more than one salt have been applied to improve both the Ca²⁺ solvation and the coulombic efficiency.^[10] Looking at other battery technologies struggling partially with the same problems, such as batteries using lithium metal anodes, the concept

of high entropy electrolytes (HEEs) has been introduced – which originates from high entropy alloys (HEAs).^[11] While HEAs are strictly based on at least five main components of roughly equiatomic composition,^[12] the concept of HEEs has been used rather freely. Some refer to their electrolytes as HEEs only by having higher entropy from mixing several electrolyte solutions,^[13,14] while other studies simply use more than one salt,^[15,16] and again other studies do both.^[17] The need for a common definition of HEEs specifically and the use of the term high entropy applied to electrolytes in general, has been commented upon recently.^[18]

Using concepts such as liquid HEEs, either solvent- or salt-based, may result in improved cyclability by enhancing electrochemical stability,^[13,14] as well as increased conductivity despite low salt concentrations.^[15] Other types of electrolytes, such as molten salt electrolytes (MSEs) have a natural entropy connection, though not necessarily high entropy. As MSEs contain only salt and thus are solvent free, combinations of two or three salts, typically around the eutectic point, are often used to counterbalance their high melting temperatures.^[19–21] Furthermore, moving from binary to ternary mixtures has resulted in higher ionic conductivities but lower cation transference numbers.^[20] In addition, just like glasses and other materials with high entropy,^[22] the MSEs are most often not at thermal equilibrium. The MSE complexity can be increased further by combining salts with different charges.^[21] As the entropic effects on different electrolyte systems vary, it is important to specify the specific type of entropy contribution. Here the entropy of mixing (ΔS_{mix}) is foremost considered, defined by,

$$\Delta S_{mix} = -nR \sum_i x_i \ln x_i \quad (1)$$

where n is the total number of moles, R is the gas constant and x_i is the molar fraction of the species i . As $\ln x_i < 0$, ΔS_{mix} is

[a] J. Timhagen, Dr. C. Cruz, Prof. J. Weidow, Prof. P. Johansson
Department of Physics
Chalmers University of Technology
SE-412 96, Gothenburg, Sweden
E-mail: patrik.johansson@chalmers.se

[b] Prof. P. Johansson
ALISTORE-European Research Institute
CNRS FR 3104, Hub de l'Énergie, 80039 Amiens, France

Supporting information for this article is available on the WWW under <https://doi.org/10.1002/batt.202400297>

© 2024 The Authors. Batteries & Supercaps published by Wiley-VCH GmbH. This is an open access article under the terms of the Creative Commons Attribution Non-Commercial License, which permits use, distribution and reproduction in any medium, provided the original work is properly cited and is not used for commercial purposes.

always >0 and depends only on the number of components, and thus all binary (as ternary, quaternary, etc.) MSEs will have the same ΔS_{mix} .

Here CaBs combined with MSEs are targeted to create HEEs using ternary and quaternary MSEs. By using calcium bis(fluorosulfonyl)imide ($\text{Ca}(\text{FSI})_2$) in combination with the analogous Li-, Na-, and KFSI salts in equimolar compositions, a high concentration of Ca^{2+} charge carriers are added but no organic compounds, which could facilitate a beneficial largely inorganic solid electrolyte interphase (SEI) at the Ca anode surface. The FSI anion is highly fluorinated and has a delocalized negative charge, and as such it is commonly used in batteries for its chemical and thermal electrolyte stability.^[23] Compared to the common alkali metal bis(trifluoromethanesulfonyl)imide (TFSI) anion, which is structurally very similar, FSI based electrolytes exhibit higher conductivities, fewer problems of aluminum corrosion^[24] and the salts have lower melting points^[19] – which is beneficial for the creation of low melting MSEs. Furthermore, as these MSEs are only limited by the salt/anion decomposition, which typically occurs at much higher temperatures than that of the boiling or flash points of the organic solvents used in liquid electrolytes, the upper temperature stability limit is typically higher.^[25,26] In addition, having only the anion(s) to consider also the electrochemical stability windows can likely be wider.

The effects of increased entropy on the stability, and on the local structure and coordination within these MSE-based HEEs are explored macroscopically by thermal gravimetric analysis (TGA) and differential scanning calorimetry (DSC) as well as locally by Raman spectroscopy. To support the interpretation of the local structure, computational techniques – molecular dynamics (MD) simulations and density functional theory (DFT) calculations – have been applied, which, as opposed to using additional experimental techniques such as nuclear magnetic resonance (NMR) spectroscopy, which both would need many nuclei to be probed and carries large practical challenges due to the high viscosities at hand, provide support to the very phenomena probed and detailed insights. Overall, the disordered and highly viscous nature of MSEs pose significant challenges for experimental techniques to capture accurate structural information.

Results and Discussion

In each section below the properties of the single salts are first outlined in order to better understand the individual contributions to the MSEs. First thermal properties are presented and the effect of Lewis acidity as well as the contribution of the entropy of mixing and partially the entropy of fusion is discussed. Subsequently, the focus falls on the local structure of both ternary and quaternary MSEs and how this connects to the global properties, such as stability.

Thermal Properties of Salts and MSEs

Starting with the TGA data analysis of the single salts, they have their $T_{d1\%}$ and $T_{d5\%}$ at (ca.) 170–200 °C and 300–320 °C, respectively (Figure 1 a, b). This is much higher than what is reported in the literature: 70–150 °C,^[27] but this could, at least partially, be attributed to the definitions used for T_d (% of mass loss), as well as the purity of the salts.^[23] The most pronounced differences occur for LiFSI, which has a mass loss of 5% at 208 °C here, but at 70 °C in the literature.^[27] The $T_{d5\%}$ increases with increased cation size^[28] – at least for the monovalent cation-based salts. The $\text{Ca}(\text{FSI})_2$, with its divalently charged Ca^{2+} , has strong ion-ion interactions that increase the T_d even further.

Continuing with the MSEs, they all decompose at (ca.) 170 °C ($T_{d1\%}$) and 300 °C ($T_{d5\%}$), in stark similarity with the single salts. As a first level approximation, it is expected that the weakest ion-ion interaction of any single salt included in the MSE, also will limit its stability.^[27] However, all MSEs have similar $T_{d5\%}$.

Turning to the DSC data of single salts, the T_m of Li-, Na-, and KFSI are all 100–140 °C (Figure 1 c–e), melting points in agreement with the literature.^[27] $\text{Ca}(\text{FSI})_2$ first appears to crystallize at 181 °C, before the onset of melting at 240 °C. The melting points largely depend on the charge/radius ratio – decreasing T_m with increased cation size, for the alkali ions. For $\text{Ca}(\text{FSI})_2$, Ca^{2+} is between Li^+ and Na^+ in terms of radius, but its divalency renders it a higher T_m .

The T_m of the MSEs is 60–75 °C for the ternary electrolytes and 54 °C for the quaternary electrolyte. The lowered melting point for the latter can be inferred to depend on its higher entropy e.g. increased ΔS_{mix} . Furthermore, the roles of differently sized cations and the tentative disorder created by these size differences can also be inferred; the MSE with the smallest ion radii differences, $[\text{CaLiNa}]\text{FSI}$, also has the highest T_m .

These melting points are a result of initial heating of crystalline powder (mixtures). After cooling down and heating the MSEs again, they only exhibit a glass transition – pointing to inherent slow dynamics and non-equilibrium, as expected. As the T_m of the MSEs with Ca^{2+} included coincide with the literature T_m values for MSEs without any Ca^{2+} ,^[27] it begs the question of whether Ca^{2+} truly is part of the MSEs created. Complementary tests of equimolar MSEs without Ca^{2+} show slightly higher T_m (Figure S1), indicating that Ca^{2+} is part of the created MSEs.

Comparing the T_m from the DSC data with the ΔS_{mix} from Eq. 1 (Figure 1 f), the Lewis acidity of the salt's cations: $\text{Ca}^{2+} > \text{Li}^+ > \text{Na}^+ > \text{K}^+$ plays a role, as the harder cations lower the melting point.

ΔS_{mix} can decrease the T_m of the quaternary MSE to 54 °C. However, the configurational entropy, partially stemming from ΔS_{fus} , does not seem to have any significant effect on the melting point (Figure S2).

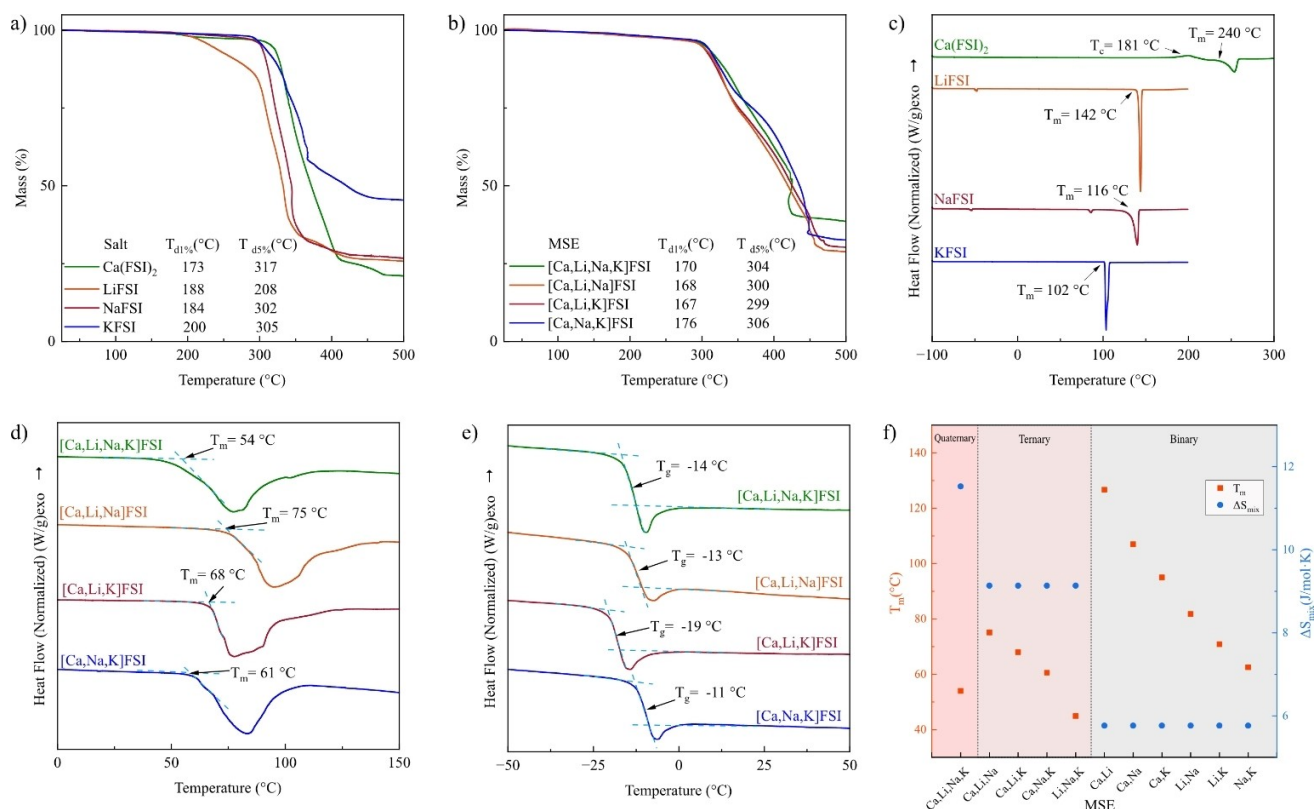


Figure 1. TGA traces of (a) single salts and (b) MSEs, with decomposition temperatures inset. DSC traces of (c) single salts, (d) ternary and quaternary MSEs - 1st heating, and (e) 2nd heating. (f) T_m and ΔS_{mix} for the, left-to-right, quaternary, ternary and binary MSEs.

Local Structure and Entropic Stabilization

Using Raman spectroscopy and the spectral range 650–850 cm^{-1} containing the FSI anion ‘all breathing mode’^[30] the cation anion interactions can be studied both for the single salts and the ternary and quaternary MSEs.^[31] While the local structure and in particular the ion-solvent interactions in a general electrolyte often are hard to determine and require tedious deconvolution to be made, the MSEs are completely solvent-free and clear bands from ion-ion interactions can be observed.

Starting with the single salts (Figure 2a), the Raman band shifts vs. a “free” FSI anion (720 cm^{-1} ^[32,33]) all shift to higher wavenumbers with a size according to the polarization power, as expected. The exception is $\text{Ca}(\text{FSI})_2$, as despite Ca^{2+} having a larger polarizing power than Li^+ does,^[34] shifts marginally less: 772 cm^{-1} for Ca^{2+} vs. 773 cm^{-1} for Li^+ (Table 1). The DFT calculated Raman spectra (Figure S3), using ion-pair and triplet models, overall supports this picture, with a maximum shift discrepancy of (ca.) 15 cm^{-1} (for LiFSI). The small band seen experimentally at 795 cm^{-1} for $\text{Ca}(\text{FSI})_2$ is left unassigned, but computationally it resembles a Ca^{2+} perturbed FSI mode.

Moving to the MSEs (Figure 2b) they all have one strong broad band centered at ca. 771 cm^{-1} and a less intense band at ca. 795 cm^{-1} (Table 2), hence an indication of the $\text{Ca}(\text{FSI})_2$ influence. Typically, when single salts with the same anion are combined into multi-cationic mixtures, the Raman spectra are

Table 1. Mode assignments for the single salts.

Salt	Mode assignment	Wavenumber [cm^{-1}]			
		Exp.	Comp. Ion/Ion-pair	Triplet	
FSI	ν_2 SNS	720	726	–	
$\text{Ca}(\text{FSI})_2$	ν_2 SNS	772	822	774	
		795	906	810	
LiFSI	ν_2 SNS	773	789	767	
NaFSI	ν_2 SNS	753	767	760	
KFSI	$\delta_{scf}\text{SO}_2 + \nu_2\text{SF}$ ^[29]	727	700	717	
		ν_2 SNS	749	790	753
		ν_2 SNS	768	860	767

expected to be simply additive, where the fraction of each salt would correspond to the overall shift of each spectrum.^[31] However, as these MSEs are charge asymmetric, it is not certain that the enthalpy of mixing is ideal, and the spectra cannot be guaranteed to be additive. The clear band at 772 cm^{-1} also has a shoulder, and broad bands and shoulders are usually signatures of disordered and local structures out of equilibrium.

The increased entropy and possible entropic stabilization of the local structure of the MSEs has been studied by recording the Raman spectra after natural aging (Figures 2c, 2d). The aged ternary MSEs have all lost the shoulder and those containing KFSI have also gained two new bands at 727 cm^{-1} and 749 cm^{-1} (Table 2), corresponding to partially (re-)crystallized /

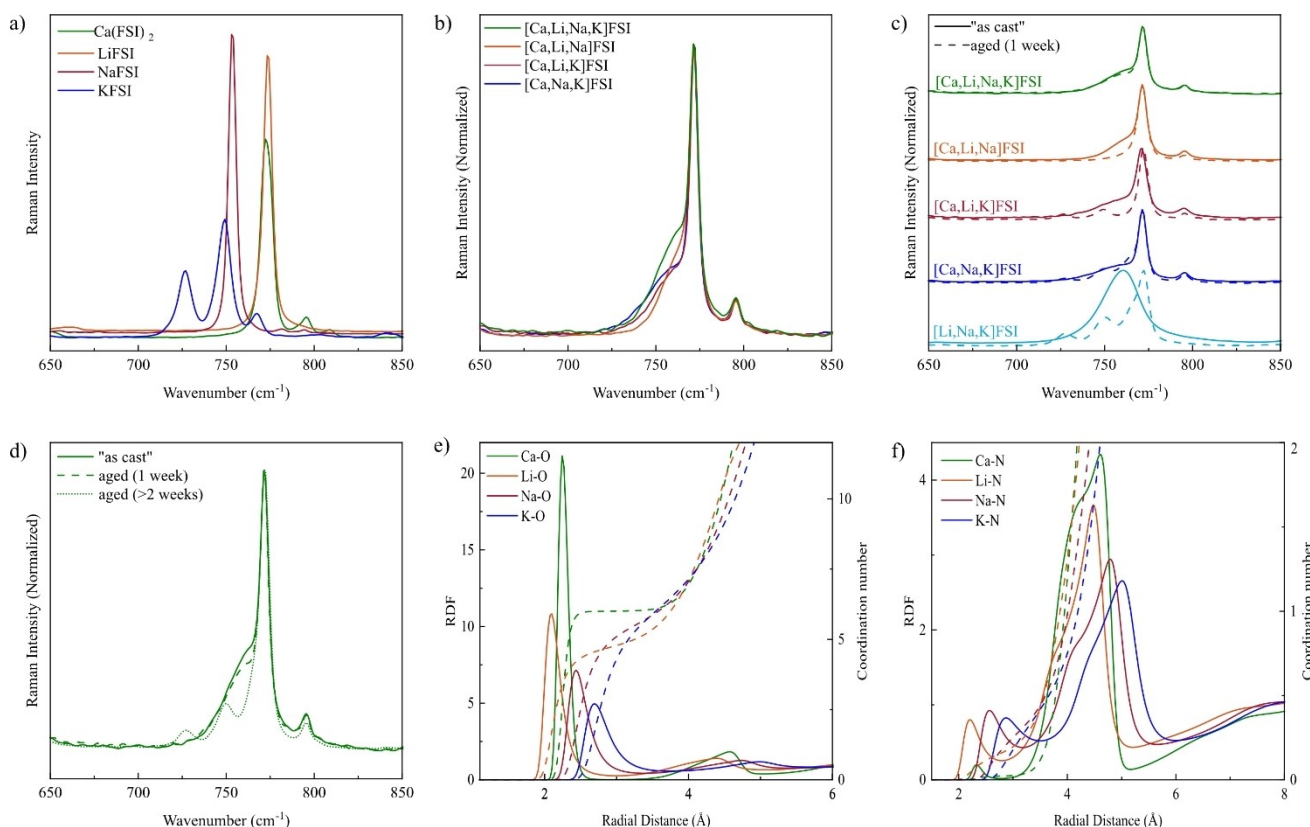


Figure 2. Raman spectra of (a) single, (b) MESS, (c) MSEs – “as cast” and aged 1 week, and (d) the quaternary [CaLiNaK]FSI MSE – “as cast” and aged, both 1 and 2 weeks, all in the spectral range 650–850 cm^{-1} . RDFs (solid lines) and cumulative coordination numbers (dashed lines) for (e) $M^{+/2+}-O$ and (f) $M^{+/2+}-N$.

Table 2. Mode assignments for the MSEs.

MSE	Mode assignment	Wavenumber [cm^{-1}]		
		As cast	Aged 1 week	Aged > 2 weeks
[CaLiNaK]FSI	$\delta_{\text{scf}}\text{SO}_2$	–	–	727
	$+\nu_5\text{SF}^{(29)}$	–	–	750
	$\nu_3\text{SNS}$	771	771	772
	$\nu_3\text{SNS}$	795	795	795
[CaLiNa]FSI	$\nu_3\text{SNS}$	771	771	–
	–	795	795	–
	–	–	–	–
[CaLiK]FSI	$\delta_{\text{scf}}\text{SO}_2$	–	727	–
	$+\nu_5\text{SF}^{(29)}$	–	749	–
	$\nu_3\text{SNS}$	771	772	–
	$\nu_3\text{SNS}$	795	795	–
[CaNaK]FSI	$\delta_{\text{scf}}\text{SO}_2$	–	727	–
	$+\nu_5\text{SF}^{(29)}$	–	750	–
	$\nu_3\text{SNS}$	771	771	–
	$\nu_3\text{SNS}$	795	795	–
[LiNaK]FSI	$\delta_{\text{scf}}\text{SO}_2$	–	728	–
	$+\nu_5\text{SF}^{(29)}$	761	750	–
	$\nu_3\text{SNS}$	761	772	–
	$\nu_3\text{SNS}$	–	–	–

micro-separated KFSI. The spectrum of the quaternary MSE, however, has not changed significantly; only after further aging (> 2 weeks) it loses its shoulder (Figure 2d). The ternary reference [LiNaK]FSI, the only MSE not containing $\text{Ca}(\text{FSI})_2$, does not even in the “as cast” state show the same sharp band at

772 cm^{-1} nor the smaller band at 795 cm^{-1} – a clear indication of the effect of $\text{Ca}(\text{FSI})_2$ on the local structure. Hence, the non-equilibrated state is not an effect of the presence of divalent Ca^{2+} , but the stabilizing effect seen for the quaternary [CaLiNaK]FSI MSE, is at least partially attributed to its higher entropy.

The local structure of the quaternary MSE was also analyzed in detail using MD simulations, where the resulting cation radial distribution functions (RDFs) (Figures 2e, 2f) reveal a relatively prominent first peak for all cations, at 1.8–3.0 Å, due to $M^{+/2+}-O$ interactions (Figure 2e) and/or $M^{+/2+}-N$ interactions, contributing to the coordination (Figure 2f). Beyond this range, the fluctuations decrease in amplitude which indicates the short-range order and medium-range disorder of the MSE. The first cation coordination shell maxima for $M^{+/2+}-O$ follow the same sequence as found above for the Raman shifts: $\text{Li}^+ < \text{Ca}^{2+} < \text{Na}^+ < \text{K}^+$.

For the $M^{+/2+}-N$ interactions the story is more complex; some/most of the FSI nitrogen atoms are in close proximity to the cations only due to the $M^{+/2+}-O$ coordination with the cations, which agrees for example with the MD simulations by Tong et al. on a LiTFSI in DMC organic electrolyte, showing coordination numbers (CNs) of 2.5 for $\text{Li}^+-O_{\text{TFSI}}$ and 0.7 for $\text{Li}^+-N_{\text{TFSI}}$ ^[35] and similarly by Li et al. for LiTFSI in acetamide.^[36]

Using slightly different cut-offs to correspond to the first minimum in each RDF for the first cation coordination shell, renders a CN trend: $\text{Li}^+ < \text{Na}^+ < \text{Ca}^{2+} < \text{K}^+$ (Table 3), where the

Salt	Coordination number $M^{+/2+}$ -O	Radial distance [Å]	Coordination mode (Monodentate:Bidentate)	Solvation number
Ca(FSI) ₂	6.0	2.9	6:0	5.9
LiFSI	4.8	3.0	3:1	4.1
NaFSI	5.7	3.4	2:2	4.3
KFSI	6.5	3.8	5:1	5.5

partial CN from $M^{+/2+}$ -N follows: $Ca^{2+} < Li^+ < Na^+ < K^+$. Hence, the variations in the cation CNs are attributed to differences in ion size. Specifically, K^+ is coordinated by more oxygen atoms due to its larger size. Furthermore, understanding the coordination mode of oxygen from the FSI around each cation provides insight into the solvation structure. While the FSI is recognized for its flexibility and therefore primarily is regarded as a bidentate ligand^[37,38] (see Figure 3a), monodentate coordination has also been suggested to contribute^[39] (see Figure 3b).

The solvation number (SN) is less straight forward to obtain than simply from the $M^{+/2+}$ -N CNs (each FSI has only one N atom), due to partial overlap of the first and second solvation shells, but also requires a larger radial cut-off than for the CNs (Figure 2f). Thus, to obtain the SNs, the first solvation shell was extrapolated to reconstruct its profile, and the cumulative number was determined at the minimum of this solvation shell (see Figure S4).

While the MD simulations offer valuable insights into the behavior of the solvent-free MSEs, it is crucial to acknowledge inherent limitations and uncertainties. The force fields used are

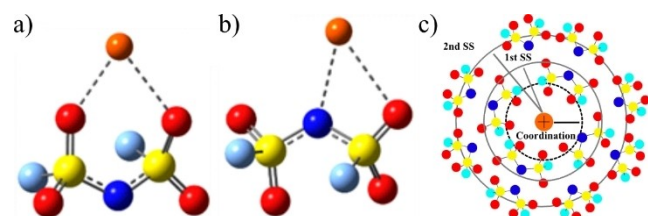


Figure 3. FSI anion coordination to a Li^+ (a) bidentately (b) monodentately, and (c) schematic of the coordination and solvation (SS: solvation shell).

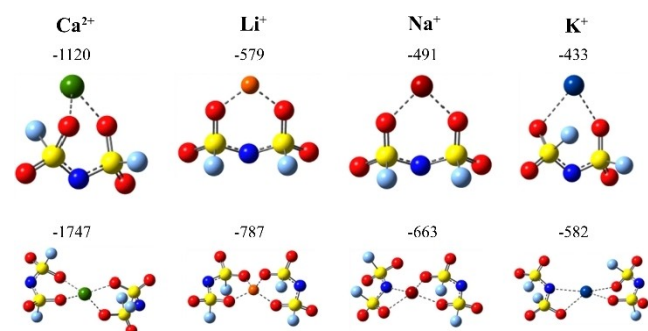


Figure 4. Local structure and binding energies [$kJmol^{-1}$] of ion-pairs and triplets.

certainly not parameterized for MSEs why transferability is arguably limited.^[40] The CL&Pol polarizable force field used was, however, initially developed for ionic liquids, protic ionic liquids, and eutectic solvents, and hence improves upon common fixed charge models,^[40] and furthermore MSEs are close enough to those materials in terms of physics, including strong Coulombic interactions, to motivate this choice of force field, despite lack of experimental validation.

DFT calculations were performed to obtain the most stable configurations of ion-pairs and triplets for each cation (Figure 4). For Li^+ and Ca^{2+} , double bidentate coordination is favored in the triplets, as previously reported for Li^+ ,^[41] while only monodentate coordination has been reported for Ca^{2+} .^[42] For Na^+ and K^+ , triplets with mixed mono and bidentate coordination are the most stable.

Concluding Remarks

The proof-of-concept oriented analyses made here demonstrate how the properties of single salts as well as the individual contributions of ions affect the local structure and entropic stabilization of Ca-based MSEs. The MSEs all show minor variations in the melting points and homogenous melting behavior, which is consistent with short-range order and medium-range disorder. Moreover, the divalent Ca^{2+} cations appear to stabilize the local structure by strong Coulombic interionic interactions. The non-equilibrated state of the MSEs, however, does not seem to be affected differently by Ca^{2+} as compared to by the monovalent cations, but rather, at least partially, be an effect of the increased entropy of mixing, as in particular seen for the quaternary MSE.

As new electrolyte design concepts are crucial in the development of non-passivating layers at the Ca metal anodes in CaBs, MSEs offer a potential solution that can translate into practical CaBs in the future. Still, as typical for MSEs, they suffer from high viscosities leading to problems in the very making of battery cells and in slow dynamics, that can translate to C-rate limitations. Electrochemical testing, ultimately needed, may require both large amounts of expensive salts, and in the case of Ca with limited availability, and elevated temperatures. The latter may in practice result in no need for an active cooling system, especially also when considering that, as opposed to liquid electrolytes, MSEs are thermally stable and non-volatile over a range of operational temperatures.

Experimental and Computational

Sample Preparation

Four different commercial salt were used; $Ca(FSI)_2$ (ProviscoCSS-r.o.,99.0%), LiFSI (Nippon ShokuBai Co.,Ltd., 99.9%), NaFSI (Solvionic,99.7%) and KFSI (Nippon ShokuBai Co., Ltd., 99.7%), where $Ca(FSI)_2$ was used as received and all other salts were dried in a vacuum Büchi oven(<7 Pa and 72 h at $80^\circ C$). For Raman spectroscopy experiments, all salts apart from the already very fine powder of NaFSI was crushed with pestle and mortar. In all other experi-

ments, the salts were used as is. Four MSEs; [CaLiNaK]FSI, [CaLiNa]FSI, [CaLiK]FSI and [CaNaK]FSI, were prepared in equimolar compositions and grinded together manually with pestle and mortar for ~15 minutes. Additional reference MSEs; [LiNaK]FSI, [CaLi]FSI, [CaNa]FSI, [CaK]FSI, [LiNa]FSI, [LiK]FSI and [NaK]FSI, were prepared similarly.

TGA

Thermal gravimetric analysis (TGA) was performed using a TG209F1 Iris from Netzsch. Hermetic alumina pans with pinholes were loaded with (ca.) 10 mg of sample and placed in the sample compartment where a nitrogen flow of 100 mLmin⁻¹ was applied. All samples were heated from 25 °C to 500 °C at a rate of 5 °Cmin⁻¹. The decomposition temperatures (T_d) were defined as the temperatures of 1% and 5% of mass loss.

DSC

Differential scanning calorimetry (DSC) was performed using a DSC250 from TA instruments. (ca.) 10 mg of the sample was hermetically sealed in an aluminum pan. For the melting points (T_m) of the single salts, the samples were cooled at 10 °Cmin⁻¹ to -100 °C, and kept there for 5 minutes, before being heated at 5 °Cmin⁻¹ up to 200 °C (apart from Ca(FSI)₂ which was heated up to 300 °C). For the T_m of the MSEs, the samples were heated up to 200 °C using a heating rate of 5 °Cmin⁻¹. For glass transition temperature (T_g) the samples were heated at 20 °Cmin⁻¹ up to 130 °C, kept there for 30 minutes, cooled down at 10 °Cmin⁻¹ to -100 °C, kept for 5 minutes, and then heated at 10 °Cmin⁻¹ up to 200 °C. The onsets of the endothermic phase transitions were used to determine the T_m and the midpoint of the step reaction of the second heating was used to determine the T_g . From the DSC experiments, the entropy of fusion (ΔS_{fus}) was estimated. By obtaining the enthalpy of fusion (ΔH_{fus}) from the area of the melting peak, and assuming that the MSEs undergo only a phase transition from solid to liquid at T_m , ΔG_{fus} , the Gibbs free energy of fusion can be set = 0, so that,

$$\Delta G_{fus} = \Delta H_{fus} - T_m \Delta S_{fus} = 0 \quad (2)$$

The ΔS_{fus} can thus be calculated as,

$$\Delta S_{fus} = \frac{\Delta H_{fus}}{T_m} \quad (3)$$

Raman Spectroscopy

Raman data were recorded using a Bruker MultiRAM FT-Raman spectrometer with a spectral resolution of 2 cm⁻¹ using a Nd : YAG laser (1064 nm, 300 mW) as an excitation source and averaged over 4000 scans. Data of single salts filled in glass vials were recorded at room temperature. Samples of MSEs were temperature controlled at 90 °C (apart from [CaNaK]FSI and [CaLiNa]FSI that were molten at 100 °C and 125 °C, respectively) and held for 1 h, before being cooled down for 1 h to room temperature, and data recorded. The MSE samples were stored in an argon-filled glovebox for 1 week and then data was once again recorded at room temperature.

MD Simulations and DFT Calculations

The MD simulations of the quaternary MSEs employed LAMMPS,^[43] the CL&Pol polarizable force field^[43-46] and a cubic simulation box containing 175 ion pairs of each salt (Figure 5), with the initial configuration created using Packmol software.^[47] The molecular topology files and the Lennard Jones and bonded parameters were generated using the fftool package.^[48]

An energy minimization employing conjugate gradients was followed by an equilibration run in the isothermal-isobaric ensemble (NPT) at 400 K and 1 atm for 1 ns. Subsequently, an additional 1 ns equilibration run was performed in the canonical ensemble (NVT) at 400 K and 1 atm. The production step was run in the canonical ensemble for 15 ns at 400 K and 1 atm, utilizing the average simulation box size obtained from the NPT equilibration run.

A Nosé-Hoover thermostat with a temperature damping of 100 fs and a pressure damping of 1000 fs was applied. Electrostatic interactions were computed using the particle-particle-particle-mesh scheme (PPPM), and periodic boundary conditions were implemented in all directions. Radial distribution functions and coordination numbers for subsequent structural analysis were obtained from LAMMPS subroutines.

In addition to the MD simulations, DFT calculations were performed in the gas phase of ion-ion interaction energies using the Gaussian software^[49] at the M06-2X/6-311G level of theory. The geometry-optimized ion-pair and triplets were confirmed as stable structures by calculating the 2nd derivatives and vibrational frequencies. The interaction energies E_{int} , zero-point energy (ZPE) corrected, were computed as,

$$E_{int} = E[M(FSI)_n]^{(1+/2+)-n} - (E(M^{+/2+}) + nE(FSI)) \quad (4)$$

where E is the electronic energy of the species, $M^{+/2+}$ is the cation (Li^+ , Na^+ , K^+ , Ca^{2+}), $n=1$ is ion-pairs, $n=2$ triplets.

Acknowledgements

The authors would like to acknowledge the financial support from the Swedish Research Council (grants #2020 – 03988 and #2021 – 00613) and VINNOVA/Batteries Sweden (BASE) (grant 2019-00064).

Conflict of Interests

The authors declare no conflict of interest.

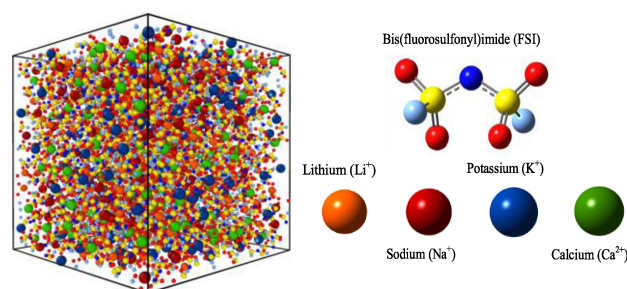


Figure 5. Schematics of the simulation box and the cations and anions.

Data Availability Statement

The data that support the findings of this study are available from the corresponding author upon reasonable request.

Keywords: molten salt electrolytes · high entropy electrolytes · calcium batteries · local structure · solvent-free electrolytes

- [1] A. Ponrouch, J. Bitenc, R. Dominko, N. Lindahl, P. Johansson, M. R. Palacin, *Energy Storage Mater.* **2019**, *20*, 253.
- [2] M. E. Arroyo-De Dompablo, A. Ponrouch, P. Johansson, M. R. Palacin, *Chem. Rev.* **2020**, *120*, 6331.
- [3] A. Ponrouch, C. Frontera, F. Bardé, M. R. Palacin, *Nat. Mater.* **2016**, *15*, 169.
- [4] D. Aurbach, R. Skaletsky, Y. Gofer, *Electrochem. Soc. Proc.* **1991**, *138*, 3536.
- [5] K. V. Nielson, T. L. Liu, *Angew. Chem. Int. Ed.* **2020**, *59*, 3368.
- [6] I. D. Hosein, *ACS Energy Lett.* **2021**, *6*, 1560.
- [7] L. Stievano, I. de Meatza, J. Bitenc, C. Cavallo, S. Brutti, M. A. Navarra, *J. Power Sources* **2021**, *482*, 228875.
- [8] H. Song, C. Wang, *Adv. En. Sust. Res.* **2022**, *3*, 2100192.
- [9] Q. Wei, L. Zhang, X. Sun, T. L. Liu, *Chem. Sci.* **2022**, *13*, 5797.
- [10] A. T. Landers, J. Self, S. A. McClary, K. J. Fritzsche, K. A. Persson, N. T. Hahn, K. R. Zavadil, *J. Phys. Chem. C* **2023**, *127*, 23664.
- [11] J. W. Yeh, S. K. Chen, S. J. Lin, J. Y. Gan, T. S. Chin, T. T. Shun, C. H. Tsau, S. Y. Chang, *Adv. Eng. Mater.* **2004**, *6*, 299.
- [12] B. S. Murty, J. W. Yeh, S. Ranganathan, P. P. Bhattacharjee, *High-Entropy Alloys*, Elsevier, **2019**.
- [13] W. Zhang, H. Xia, Z. Zhu, Z. Lv, S. Cao, J. Wei, Y. Luo, Y. Xiao, L. Liu, X. Chen, *CCS Chemistry* **2020**, *3*, 1245.
- [14] S. C. Kim, J. Wang, R. Xu, P. Zhang, Y. Chen, Z. Huang, Y. Yang, Z. Yu, S. T. Oyakhire, W. Zhang, L. C. Greenburg, M. S. Kim, D. T. Boyle, P. Sayavong, Y. Ye, J. Qin, Z. Bao, Y. Cui, *Nat. Energy* **2023**, *8*, 814.
- [15] Q. Wang, C. Zhao, J. Wang, Z. Yao, S. Wang, S. G. H. Kumar, S. Ganapathy, S. Eustace, X. Bai, B. Li, M. Wagemaker, *Nat. Commun.* **2023**, *14*, 440.
- [16] C. Yang, J. Xia, C. Cui, T. P. Pollard, J. Vatamanu, A. Faraone, J. A. Dura, M. Tyagi, A. Kattan, E. Thimsen, J. Xu, W. Song, E. Hu, X. Ji, S. Hou, X. Zhang, M. S. Ding, S. Hwang, D. Su, Y. Ren, X. Q. Yang, H. Wang, O. Borodin, C. Wang, *Nat Sustain* **2023**, *6*, 325.
- [17] Q. Wang, C. Zhao, Z. Yao, J. Wang, F. Wu, S. G. H. Kumar, S. Ganapathy, S. Eustace, X. Bai, B. Li, J. Lu, M. Wagemaker, *Adv. Mater.* **2023**, *35*, 2210677.
- [18] B. Ouyang, Y. Zeng, *Nat. Commun.* **2024**, *15*, 973.
- [19] T. Nohira, *Electrochemistry* **2020**, *88*, 477.
- [20] V. Giordani, D. Tozier, H. Tan, C. M. Burke, B. M. Gallant, J. Uddin, J. R. Greer, B. D. McCloskey, G. V. Chase, D. Addison, *J. Am. Chem. Soc.* **2016**, *138*, 2656.
- [21] Q. Pang, J. Meng, S. Gupta, X. Hong, C. Yuen Kwok, J. Zhao, Y. Jin, L. Xu, O. Karahan, Z. Wang, S. Toll, L. Mai, L. F. Nazar, M. Balasubramanian, B. Narayanan, D. R. Sadoway, *Nature* **2022**, *608*, 704.
- [22] J. W. E. Drewitt, L. Hennet, D. R. Neuville, *Rev. Mineral. Geochem.* **2022**, *87*, 55.
- [23] M. Kerner, N. Plylahan, J. Scheers, P. Johansson, *RSC Adv.* **2016**, *6*, 23327.
- [24] H. B. Han, S. S. Zhou, D. J. Zhang, S. W. Feng, L. F. Li, K. Liu, W. F. Feng, J. Nie, H. Li, X. J. Huang, M. Armand, Z. Bin Zhou, *J. Power Sources* **2011**, *196*, 3623.
- [25] K. Kubota, T. Nohira, R. Hagiwara, *Electrochim. Acta* **2012**, *66*, 320.
- [26] M. C. Vu, P. Mirmira, R. J. Gomes, P. Ma, E. S. Doyle, H. S. Srinivasan, C. V. Amanchukwu, *Matter* **2023**, *6*, 4357.
- [27] K. Kubota, T. Nohira, R. Hagiwara, *J. Chem. Eng. Data* **2010**, *55*, 3142.
- [28] K. Kubota, T. Nohira, T. Goto, R. Hagiwara, *J. Chem. Eng. Data* **2008**, *53*, 2144.
- [29] K. Matsumoto, T. Oka, T. Nohira, R. Hagiwara, *Inorg. Chem.* **2013**, *52*, 568.
- [30] J. Grondin, J. C. Lassègues, D. Cavagnat, T. Buffeteau, P. Johansson, R. Holomb, *J. Raman Spectrosc.* **2011**, *42*, 733.
- [31] G. J. Janz, D. W. James, *J. Chem. Phys.* **1961**, *35*, 739.
- [32] K. Kimura, J. Motomatsu, Y. Tominaga, *J. Phys. Chem. C* **2016**, *120*, 12385.
- [33] J. Wang, Y. Yamada, K. Sodeyama, C. H. Chiang, Y. Tateyama, A. Yamada, *Nat. Commun.* **2016**, *7*, 12032.
- [34] D. S. Tchitchekova, D. Monti, P. Johansson, F. Bardé, A. Randon-Vitanova, M. R. Palacin, A. Ponrouch, *J. Electrochem. Soc.* **2017**, *164*, 1384.
- [35] J. Tong, X. Xiao, X. Liang, N. Von Solms, F. Huo, H. He, S. Zhang, *Phys. Chem. Chem. Phys.* **2019**, *21*, 19216.
- [36] S. Li, Z. Cao, Y. Peng, L. Liu, V. Wang, S. Wang, J. Q. Wang, T. Yan, X. P. Gao, D. Y. Song, P. W. Shen, *J. Phys. Chem. B* **2008**, *112*, 6398.
- [37] S.-D. Han, O. Borodin, D. M. Seo, Z.-B. Zhou, W. A. Henderson, *J. Electrochem. Soc.* **2014**, *161*, A2042.
- [38] L. Wang, Z. Luo, H. Xu, N. Piao, Z. Chen, G. Tian, X. He, *RSC Adv.* **2019**, *9*, 41837.
- [39] O. Borodin, G. D. Smith, W. Henderson, *J. Phys. Chem. B* **2006**, *110*, 16879.
- [40] M. A. González, *École Thém. Soc. Fran. Neutron.* **2011**, *12*, 169.
- [41] K. Angenendt, P. Johansson, *J. Phys. Chem. B* **2011**, *115*, 7808.
- [42] J. Z. Hu, N. R. Jaegers, N. T. Hahn, W. Hu, K. S. Han, Y. Chen, J. A. Sears, V. Murugesan, K. R. Zavadil, K. T. Mueller, *JACS Au* **2022**, *2*, 917.
- [43] S. Plimpton, *J. Comput. Phys.* **1995**, *117*, 1.
- [44] K. Goloviznina, Z. Gong, A. A. H. Padua, *Wiley Interdiscip. Rev.: Comput. Mol. Sci.* **2022**, *12*, 1.
- [45] R. Maglia De Souza, M. Karttunen, M. C. C. Ribeiro, *J. Chem. Inf. Model.* **2021**, *61*, 5938.
- [46] K. Goloviznina, J. N. Canongia Lopes, M. Costa Gomes, A. A. H. Pádua, *J. Chem. Theory Comput.* **2019**, *15*, 5858.
- [47] L. Martinez, R. Andrade, E. G. Birgin, J. M. Martinez, *J. Comput. Chem.* **2009**, *30*, 2157.
- [48] A. A. H. Pádua, *J. Chem. Phys.* **2017**, *146*, DOI 10.1063/1.4983687.
- [49] M. J. Frisch, G. W. Trucks, H. B. Schlegel, G. E. Scuseria, M. a. Robb, J. R. Cheeseman, G. Scalmani, V. Barone, G. a. Petersson, H. Nakatsuji, X. Li, M. Caricato, a. V. Marenich, J. Bloino, B. G. Janesko, R. Gomperts, B. Menucci, H. P. Hratchian, J. V. Ortiz, A. F. Izmaylov, J. L. Sonnenberg, Williams, F. Ding, F. Lipparini, F. Egidi, J. Goings, B. Peng, A. Petrone, T. Henderson, D. Ranasinghe, V. G. Zakrzewski, J. Gao, N. Rega, G. Zheng, W. Liang, M. Hada, M. Ehara, K. Toyota, R. Fukuda, J. Hasegawa, M. Ishida, T. Nakajima, Y. Honda, O. Kitao, H. Nakai, T. Vreven, K. Throssell, J. A. Montgomery Jr., J. E. Peralta, F. Ogliaro, M. J. Bearpark, J. J. Heyd, E. N. Brothers, K. N. Kudin, V. N. Staroverov, T. a. Keith, R. Kobayashi, J. Normand, K. Raghavachari, a. P. Rendell, J. C. Burant, S. S. Iyengar, J. Tomasi, M. Cossi, J. M. Millam, M. Klene, C. Adamo, R. Cammi, J. W. Ochterski, R. L. Martin, K. Morokuma, O. Farkas, J. B. Foresman, D. J. Fox, Gaussian 16 Revision C.01, **2016**, URL <https://gaussian.com/>.

Manuscript received: May 24, 2024
Accepted manuscript online: May 31, 2024
Version of record online: July 11, 2024